Available online at www.sciencedirect.com
ScienceDirect
Journal of Sound and Vibration 305 (2007) 97–115
JOURNAL OF SOUND AND VIBRATION
www.elsevier.com/locate/jsvi

On the instability and the post-critical behaviour of two-dimensional cantilevered flexible plates in axial flow

Liaosha Tang*, Michael P. Païdoussis

Department of Mechanical Engineering, McGill University, 817 Sherbrooke St. W., Montréal, Québec, Canada H3A 2K6

Received 3 June 2006; received in revised form 12 January 2007; accepted 20 March 2007

Abstract

This paper deals with the dynamics of a cantilevered plate subject to axial flow on both surfaces, directed from the clamped to the free end. The system loses stability by flutter, a well known fact, but the mechanism of which is insufficiently well understood. In this paper, a relatively simple numerical model is constructed for examining the instability and the post-critical behaviour of this fluid–structure system: a nonlinear equation of motion of the plate is developed using the inextensibility condition; also, an unsteady lumped vortex model is used to calculate the pressure difference across the plate. The analysis of the system dynamics is carried out in the time-domain. Both the instability and the post-critical behaviour of the system are studied. Various factors that may influence the system dynamics such as material damping, the length of the rigid upstream segment and the viscous drag are discussed in detail. A model of the wake evolution is proposed to explain the hysteresis phenomenon observed in experiments. The flutter boundary and the vibration modes predicted by the current theory are found to be in good agreement with published experimental data.

1. Introduction

A cantilevered plate immersed in an otherwise uniform axial flow may lose stability at high enough flow velocity by flutter. An everyday example of this phenomenon is the waving motion of flags in the wind. Obviously, this is a fluid–structure interaction problem. It is now generally understood that the flutter of the fluid–structure system in question is a self-excited phenomenon; it is not caused by vortex shedding from the upstream support, nor is it a Kelvin–Helmholtz instability [1,2]. Although this problem appears to be simple at first glance, it is indeed a challenging one if one considers the vortical wake discharging from the trailing edge of the plate and the large amplitude and high frequency of the ensuing flutter.

As shown in Fig. 1, cantilevered plates in axial flow may have vertical, horizontal or hanging configurations. How the gravitational force acts on the plate is the only difference among these configurations. The geometrical characteristics of a rectangular homogeneous plate are the length of the flexible section L, width B and thickness h. Normally, there is a rigid segment of length L_0 as part of the clamping arrangement at the upstream end. The other physical parameters of the system are: the plate material density ρ_P and bending

*Corresponding author. Tel.: +1 514 3986290; fax: +1 514 3987365.
E-mail address: liaosha.tang@mail.mcgill.ca (L. Tang).

0022-460X/$ - see front matter
doi:10.1016/j.jsv.2007.03.042

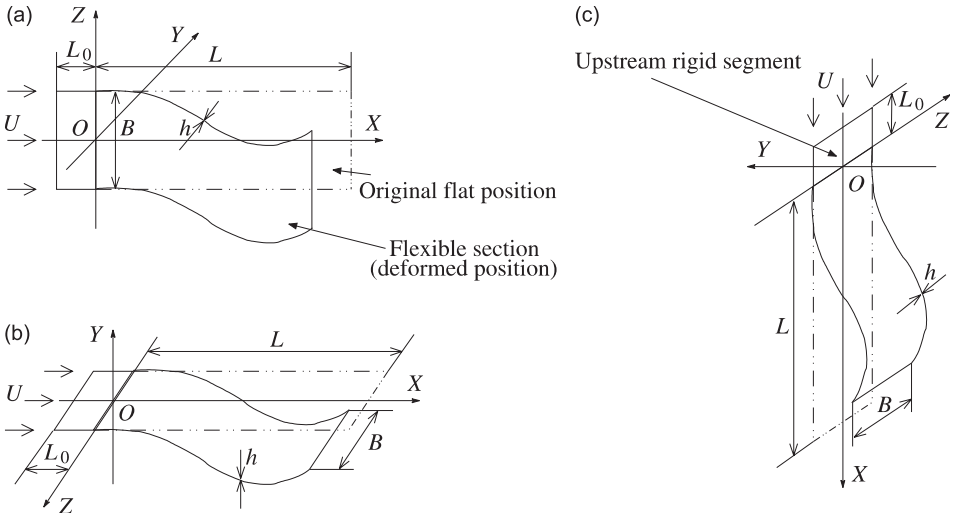

Fig. 1. Three configurations of cantilevered plates in axial flow: (a) vertical, (b) horizontal, and (c) hanging.

stiffness $D = Eh^3/[12(1-\nu^2)]$, where E and ν are, respectively, Young's modulus and the Poisson ratio of the plate material, the fluid density ρ_F, and the undisturbed flow velocity U. The plate may be called a flag, a sheet, or specifically a two-dimensional plate, when the aspect ratio B/L is large. Conversely, it may be called a strip when the aspect ratio is small. Historically, the terms *flag* and *strip* were frequently used to refer to a structure with perfect flexibility. However, these terminologies are interchangeable with *plate* when the bending stiffness, no matter how small, is taken into account.

Since the dynamics of plates in flow is indeed a huge topic, we need to delimit the type of system considered, for the purposes of the literature review which follows. Firstly, the structure is considered to be a single flexible plate of finite length. Secondly, the plate is clamped at its upstream edge; all the other edges are free. Thirdly, the fluid passes over both surfaces of the plate in the direction from the clamped leading edge to the free trailing edge; no cross-flow is considered. Finally, the plate is thin and very pliable; hence flutter is expected at low flow velocities.

Plate flutter has been studied for a long time. An excellent early monograph on this topic was published by Dowell [3]. A recent review is also available in the book by Païdoussis [4].

Taneda [5] investigated flag flutter in a series of carefully conducted experiments; his work may be the earliest one on flags and strips in the hanging configuration. Datta and Gottenberg [6] conducted similar experiments on strip flutter and tried to give theoretical predictions of the critical flow velocity U_c in terms of strip thickness and length; the strip was modelled as a cantilevered beam, and slender wing theory [7] was used in the evaluation of the aerodynamic loads. Interesting experiments on hanging filaments in a flowing soap film were conducted by Zhang et al. [1]; one of the important observations made was in regard of the evolution of the wake vortices and its correlation to system stability. Hanging strips were recently studied afresh by Yadykin et al. [8] using a nonlinear beam model based on the inextensibility condition [9] and slender wing theory for the aerodynamics. The latest work on strip flutter was undertaken by Lemaitre et al. [10], who focused on the possible independence of the critical flow velocity U_c on strip length if the latter is sufficiently large, as observed in their experiments; a linear beam model and slender wing theory were used in their theoretical analysis.

In the hanging configuration, a major source of axial tension is gravity. In the vertical and horizontal configurations, however, the effects of gravity are normally neglected, and so the two arrangements in Fig. 1(a,b) may be considered to be identical.

Kornecki et al. [11] may have been the first to study plates in axial flow in a vertical/horizontal configuration. They used a linear beam model for the structure and Theodorsen's theory [12] for the aerodynamics. The influence on the critical flow velocity U_c and frequency f_c of the circulatory and non-circulatory parts of the

aerodynamic forces were discussed and correlated to their own experimental results. An extension of their theoretical work was made by Shayo [13] for plates of finite width B.

Cantilevered plates in axial flow were investigated by Huang [14] and Balint and Lucey [15] for the purpose of describing, and suggesting treatment for, human snoring caused by flutter of the soft palate. Huang did experiments and developed an analytical model using Theodorsen's theory combined with a linear beam model to predict the critical flow velocity U_c and frequency f_c. Balint and Lucey, on the other hand, coupled a linear beam model with a Navier–Stokes solver.

Guo and Païdoussis [16] examined the problem in question in their work on plates in axial flow with different upstream/downstream structural boundary conditions. They used a linear beam model and obtained the fluid loads through a direct solution of the potential flow surrounding the plate.

Cantilevered plates in axial flow were studied by Yamaguchi et al. [17], Yamaguchi et al. [18], Watanabe et al. [19] and Watanabe et al. [20] in order to obtain a better understanding of sheet flutter phenomena, widely observed in the operation of printing presses and paper machines. Both sets of researchers separately conducted a large number of experiments to explore the relation between the critical flow velocity U_c and certain system parameters. In their theoretical work, both Yamaguchi et al. [18] and Watanabe et al. [20] adopted a linear beam model for the structure. However, Yamaguchi et al. used a linearly varying vortex model together with a shedding wake to solve the lifting surface problem; Watanabe et al. used Theodorsen's theory. Moreover, Watanabe et al. also coupled their structural model with a two-dimensional compressible Navier–Stokes solver to obtain a few reference results for their analysis.

Tang et al. [21] conducted experiments and used a nonlinear structural model, making use of the inextensibility condition, to study cantilevered plates in axial flow. They used a vortex lattice model [7] to calculate the aerodynamic lift over the plate. This work was extended theoretically by Attar et al. [22] to take into account nonlinearities in the vortex lattice model.

Argentina and Mahadevan [2] investigated the flutter mechanism of cantilevered plates in axial flow by means of a linear beam model and a simplified analytical model based on Theodorsen's theory for the fluid flow. Finally, Shelley et al. [23] conducted experiments in water flow and predicted the flutter boundary by means of a linear beam model and the localized excitation theory proposed by Crighton and Oswell [24] for the fluid loads.

In this paper, we study the dynamics of two-dimensional plates in axial flow in the vertical/horizontal configuration (Fig. 1(a,b)). It is supposed that the plate width B is infinite; both the plate and the flow surrounding the plate are thus two-dimensional. Although three-dimensional flutter was reported by Taneda [5], its existence *de facto* became significant only when the structure flapped wildly at relatively high flow velocities. On the other hand, it was observed in the experiments by Datta and Gottenberg [6], Kornecki et al. [11], Huang [14], Yamaguchi et al. [18], Yadykin et al. [8], Watanabe et al. [19], Tang et al. [21] and Shelley et al. [23] that the spanwise deformation of the structure was very small, at least in a considerable range of flow velocities beyond the critical point, thus showing that the two-dimensional assumption is reasonable.

To account for large-amplitude vibrations, a nonlinear equation of motion of the plate is developed using the inextensibility condition. Material damping is considered to be of the Kelvin–Voigt type [25]. The fluid is supposed to be inviscid and incompressible, and an unsteady lumped vortex model [7] is used to calculate the pressure difference across the plate. In this model, wake shedding from the plate trailing edge is considered, using a time-stepping scheme. The pressure difference is decomposed into a lift force and an inviscid drag force. These fluid loads, together with a viscous drag separately modelled, are coupled with the equation of motion of the plate, which is then discretized via the Galerkin method. The model developed in this paper is quite similar to those by Tang et al. [21] and Attar et al. [22] but introduces certain improvements, notably by taking into account (i) the effect of tension (induced by both inviscid and viscous forces) and (ii) longitudinal displacements (''contraction'') of the plate associated with large lateral oscillations.

With the numerical model developed, extensive simulations have been carried out. The analysis is in the time-domain, and both the instability and the post-critical behaviour of the fluid–structure system are studied. The influence of the rigid upstream segment, material damping and viscous drag on the system dynamics are examined. A flutter boundary is obtained in terms of critical flow velocity U_c versus plate length L.

The current simulation results are compared with published experimental observations and predictions made by other theories.

2. Modelling and numerical methodology

2.1. Equation of motion of the plate

The post-critical motions of the plate may be of large amplitude. To account for such large deformations, a proper nonlinear model should be used. Since it is supposed to be very thin, i.e., $h \ll L$, the two-dimensional plate can be considered as a classical Euler–Bernoulli beam. Moreover, the strain level in the plate is supposed to be sufficiently small for the centreline length to be considered constant during deformation. Based on this inextensibility condition and following Semler et al. [9], the partial differential equation governing plate motion is found to be

$$\begin{aligned}&\rho_P h\ddot{W} + D\left(1 + a\frac{\partial}{\partial t}\right)[W''''(1 + W'^2) + 4W'W''W''' + W''^3] \\ &\quad + \rho_P h W' \int_0^S (\dot{W}'^2 + W'\ddot{W}')\,\mathrm{d}S - \rho_P h W'' \int_S^L \left[\int_0^S (\dot{W}'^2 + W'\ddot{W}')\,\mathrm{d}S\right]\mathrm{d}S \\ &= F_L - W'F_D + W'' \int_S^L F_D\,\mathrm{d}S, \end{aligned} \tag{1}$$

$$V = -\frac{1}{2}\int_0^S W'^2\,\mathrm{d}S, \tag{2}$$

where, as shown in Fig. 2, W and V are, respectively, the transverse and longitudinal displacements of the plate; S is the distance of a material point on the plate from the origin, measured along the plate centreline in a coordinate system embedded in the plate; F_L and F_D are, respectively, the transverse and longitudinal fluid loads acting on the plate; a is the material damping coefficient, assuming a Kelvin–Voigt model [25]. The overdot and the prime, respectively, represent temporal and spatial derivatives, i.e., $\partial(\,)/\partial t$ and $\partial(\,)/\partial S$. Note that both Eqs. (1) and (2) are accurate to $\mathcal{O}(W'^3)$.

It should be mentioned that a one-dimensional equation of motion of the plate, i.e., Eq. (1), is obtained using the inextensibility condition; Eq. (2) is used to recover the deformed shape of the plate in the fixed X–Y coordinate system. Moreover, utilizing the relationship $\ddot{V} = \int_0^S (\dot{W}'^2 + W'\ddot{W}')\,\mathrm{d}S$ (see Ref. [9]), Eq. (1) may be rewritten as

$$\rho_P h\ddot{W} + D\left(1 + a\frac{\partial}{\partial t}\right)[W''''(1 + W'^2) + 4W'W''W''' + W''^3] - (TW')' = F_L, \tag{3}$$

where T is the tension in the plate, defined by

$$T = \int_S^L (F_D - \rho_P h\ddot{V})\,\mathrm{d}S. \tag{4}$$

That is, although the plate is assumed to be inextensible, tension still exists in it, originating from the longitudinal fluid loading as well as the inertia force of the plate in the longitudinal direction.

Using non-dimensional variables defined as

$$x = \frac{X}{L}, \quad y = \frac{Y}{L}, \quad v = \frac{V}{L}, \quad w = \frac{W}{L}, \quad s = \frac{S}{L}, \quad \tau = \frac{t}{\sqrt{\rho_P h L^4/D}},$$

$$f^\star = f\sqrt{\rho_P h L^4/D}, \quad \alpha = \frac{a}{\sqrt{\rho_P h L^4/D}}, \quad f_L = \frac{F_L}{\rho_F U^2}, \quad f_D = \frac{F_D}{\rho_F U^2}, \tag{5}$$

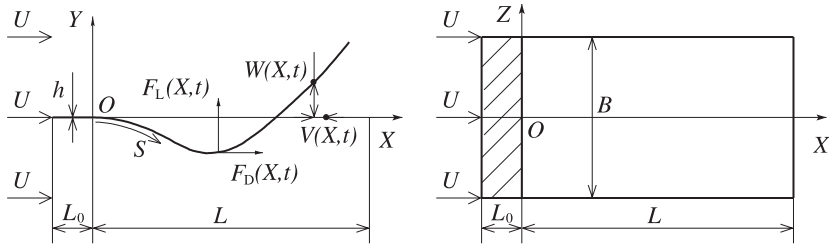

Fig. 2. A cantilevered plate in axial flow.

where $f^\star$ and f are, respectively, non-dimensional and dimensional vibration frequencies, Eqs. (1) and (2) become

$$\ddot{w} + \left(1 + \alpha\frac{\partial}{\partial\tau}\right)[w''''(1+w'^2) + 4w'w''w''' + w''^3] + w'\int_0^s (\dot{w}'^2 + w'\ddot{w}')\,\mathrm{d}s - w''\int_s^1 \left[\int_0^s (\dot{w}'^2 + w'\ddot{w}')\,\mathrm{d}s\right]\mathrm{d}s = \mu U_R^2\left(f_L - w'f_D + w''\int_s^1 f_D\,\mathrm{d}s\right), \tag{6}$$

$$v = -\frac{1}{2}\int_0^s w'^2\,\mathrm{d}s, \tag{7}$$

where the overdot and the prime from now on represent $\partial(\,)/\partial\tau$ and $\partial(\,)/\partial s$, respectively. In the non-dimensionalization, the length of the flexible segment of the plate has been used as the length scale and the characteristic time of free vibration of the plate as the time scale, i.e., the *solid time scale* $T_S = \sqrt{\rho_P h L^4/D}$. Note that there is another time scale, the *fluid time scale*, defined as $T_F = L/U$. The ratio of these two time scales is the reduced flow velocity

$$U_R = \frac{T_S}{T_F} = UL\sqrt{\frac{\rho_P h}{D}}. \tag{8}$$

Normally, when $U_R \gg 1$, it can be assumed that the response of the fluid flow due to the deformation of the plate is much faster than the motion of the plate itself; it is not necessary to take into account time-delay effects. Moreover, of major importance is the mass ratio μ defined by

$$\mu = \frac{\rho_F L}{\rho_P h}. \tag{9}$$

2.2. Model of the fluid flow

The flow velocity U is supposed to be low enough when flutter takes place for the fluid to be assumed to be incompressible. Also, for simplicity, the flow can initially be considered to be inviscid; however, the effect of viscosity will be incorporated in the drag F_D empirically as a surface viscous force. Under these conditions, the panel method, in particular the unsteady lumped vortex model, is used to predict the aero/hydrodynamics, as illustrated in Fig. 3.

The flexible section of the plate is evenly divided into N panels, each of length $\Delta s = 1/N$. Individual panels are put on the deformed contour of the plate centreline. The bound vortices, γ_1 through γ_N, together with the instantaneously formed wake vortex γ_{N+1} at a given instant, say time step $k+1$, are obtained from the

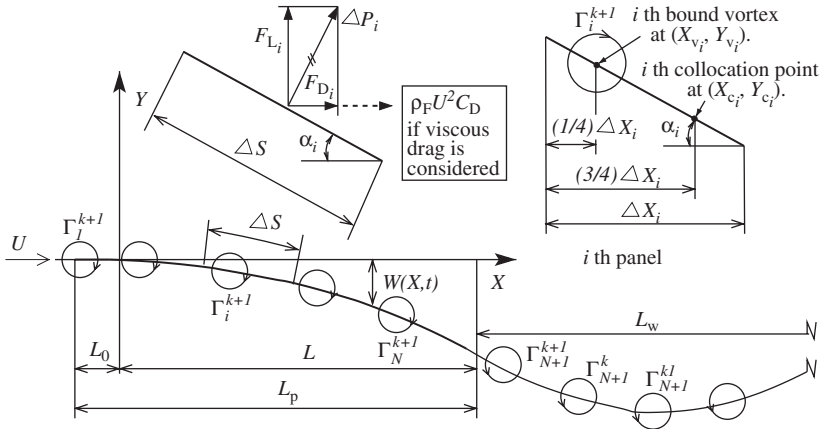

Fig. 3. The panel method applied to a cantilevered plate in axial flow.

following equations:

$$\begin{bmatrix} \alpha_{11} & \alpha_{12} & \cdots & \alpha_{1N} & \alpha_{1,N+1} \\ \alpha_{21} & \alpha_{22} & \cdots & \alpha_{2N} & \alpha_{2,N+1} \\ \vdots & \vdots & \ddots & \vdots & \vdots \\ \alpha_{N1} & \alpha_{N2} & \cdots & \alpha_{NN} & \alpha_{N,N+1} \\ 1 & 1 & \cdots & 1 & 1 \end{bmatrix} \begin{Bmatrix} \gamma_1 \\ \gamma_2 \\ \cdots \\ \gamma_N \\ \gamma_{N+1} \end{Bmatrix} = \begin{Bmatrix} \mathrm{rhs}_1 \\ \mathrm{rhs}_2 \\ \cdots \\ \mathrm{rhs}_N \\ \gamma^\star \end{Bmatrix}, \tag{10}$$

where the influence coefficients α_{ij} and the right-hand side $[\mathrm{rhs}_i, \gamma^\star]^{\mathrm{T}}$ are given by

$$\alpha_{ij} = \frac{(y_{C_i} - y_{V_j})\sin\alpha_i + (-x_{C_i} + x_{V_j})\cos\alpha_i}{2\pi[(y_{C_i} - y_{V_j})^2 + (x_{C_i} - x_{V_j})^2]}, \tag{11}$$

$$\mathrm{rhs}_i = \left(\frac{\dot{v}_i}{U_R} - 1 - v_{W_i}\right)\sin\alpha_i + \left(\frac{\dot{w}_i}{U_R} - w_{W_i}\right)\cos\alpha_i, \tag{12}$$

$$\gamma^{\star k+1} = \sum_{i=1}^{N} \gamma_i^k. \tag{13}$$

In Eqs. (10), $\gamma_{i,i=1,2,\ldots,N}$ and γ_{N+1} are, respectively, the strengths of the bound vortices $\Gamma_{i,i=1,2,\ldots,N}$ and the latest wake vortex Γ_{W_1} normalized by UL. In Eqs. (11) and (12), $(x,y)_{C_i}$ and $(x,y)_{V_i}$ are, respectively, the coordinates of the bound vortex and the collocation point on the ith panel $(X, Y)_{C_i}$ and $(X, Y)_{V_i}$ normalized by L; $(v,w)_{W_i}$ is the wake-induced velocity at the ith collocation point $(V, W)_{W_i}$ normalized by the undisturbed flow velocity U. In Eq. (13), the superscript $k+1$ represents the current time step; it has been dropped for clarity in Eqs. (10)–(12).

The plate is supposed to be initially held in place with a slightly deformed shape. It is then released, and fresh wake vortices are formed and shed off the trailing edge of the plate. The latest wake vortex is assumed to be born on the prolongation of the last panel and to have a longitudinal clearance of $0.25U_R\Delta\tau$ from the trailing edge, where $\Delta\tau$ is the non-dimensional time step. For simplicity, it is assumed that the movement of each individual wake vortex is not affected by the bound vortices or the other wake vortices. Therefore, they travel downstream with the same velocity as the undisturbed flow; the longitudinal distance between two neighbouring wake vortices is always $U_R\Delta\tau$.

The shape of the wake street is shown in Fig. 3. In previous studies, slender wing theory (a localized excitation theory) was often utilized, and the wake was explicitly neglected when considering low aspect ratio plates, e.g., by Datta and Gottenberg [6], Yadykin et al. [8] and Lemaitre et al. [10]. Wake effects were not

considered either in the direct solution of the potential flow problem by neither Guo and Païdoussis [16] nor in the studies of Shelley et al. [23] based on localized excitation theory. On the other hand, Theodorsen's theory was adopted by Kornecki et al. [11], Shayo [13], Huang [14] and Watanabe et al. [20], and a flat wake on the extension plane of the plate was considered to satisfy the Kutta condition at the plate trailing edge. A vortex sheet model and a vortex lattice model were respectively used by Yamaguchi et al. [17] and Tang et al. [21]; in their implementation, the wake was constrained to be along the neutral plane. An improvement was made by Attar et al. [22]; a vortex lattice model was again used and the wake vortices were considered to be free to move in the local flow field.

As shown in Fig. 3, the truncated wake street is assumed to have a normalized longitudinal length l_W, and the total number of wake vortices N_W can be determined by $N_W = l_W/(U_R\Delta\tau)$. Thus, the wake-induced velocity at the ith collocation point is calculated by

$$(v, w)_{W_i} = \sum_{j=1}^{N_W} \frac{\gamma_{W_j}}{2\pi} \frac{(y_{C_i} - y_{W_j}, -x_{C_i} + x_{W_j})}{(y_{C_i} - y_{W_j})^2 + (x_{C_i} - x_{W_j})^2}, \tag{14}$$

where γ_{W_j} and $(x, y)_{W_j}$ are, respectively, the strength and coordinates of the jth wake vortex Γ_{W_j} normalized by UL and $(X, Y)_{W_j}$ by L.

When discrete vortices γ_1 through γ_{N+1} are available at the current time step, Δp_i, the pressure difference at the ith panel (ΔP_i normalized by $\rho_F U^2$), can be calculated by the following expression [7]:

$$\Delta p_i = \left[\left(-\frac{\dot{v}_i}{U_R} + 1 + v_{W_i}\right)\cos\alpha_i + \left(\frac{\dot{w}_i}{U_R} - w_{W_i}\right)\sin\alpha_i\right]\frac{\gamma_i}{\Delta s} + \frac{1}{U_R}\frac{\partial}{\partial\tau}\left(\sum_{j=1}^{i}\gamma_j\right). \tag{15}$$

Consequently, the distributions of the lift f_{L_i} and the inviscid drag f_{D_i} over the ith panel are obtained by

$$(f_{L_i}, f_{D_i}) = \Delta p_i(\cos\alpha_i, \sin\alpha_i). \tag{16}$$

Eq. (16) gives the drag resulting only from the pressure difference across the plate; it is an inviscid drag. There is no available theory for the viscous drag acting on a plate undergoing oscillations. One approach for including viscous drag in the model is to use a Blasius-type solution, for either the laminar or the turbulent case, as a first approximation. However, it was found through extensive tests that the viscous drag calculated using the Blasius-type solution has a negligible effect on the system dynamics (as confirmed by the work of Lemaitre et al. [10]), although the results by the present theory do not entirely concur, as will be seen in Section 3.3. In this paper, a non-dimensional drag coefficient C_D is used for the drag acting on the plate due to the viscous effects of the fluid flow, the effective drag caused by viscous stresses acting on the plate and/or flow separation. An additional uniform distribution of longitudinal force given by $\rho_F U^2 C_D$ is thus assumed to act on the plate for simplicity, and the term f_{D_i} in Eq. (16) becomes

$$f_{D_i} = \Delta p_i \sin\alpha_i + C_D. \tag{17}$$

2.3. Discretization of the equation of motion of the plate

The traditional Galerkin method is applied to Eq. (6) by assuming that the plate transverse deformation can be expanded in terms of generalized coordinates $q_m(\tau)$ and the linear *in vacuo* cantilevered beam eigenfunctions $\phi_m(x)$ as

$$w(x, \tau) = \sum_{m=1}^{M} q_m(\tau)\phi_m(x), \tag{18}$$

where M is the number of modes utilized in the analysis. Eq. (6) thus becomes

$$\begin{aligned}\ddot{q}_i + A_i q_i + \alpha A_i \dot{q}_i + B_{imnl} q_m q_n q_l + \alpha B_{imnl}(\dot{q}_m q_n q_l + q_m \dot{q}_n q_l + q_m q_n \dot{q}_l) \\ + C_{imnl} q_m(\dot{q}_n \dot{q}_l + q_n \ddot{q}_l) = f_i,\end{aligned} \tag{19}$$

where Einstein's scientific notation has been used, and the range of all indices i, l, m and n is from 1 to M. The generalized load f_i is given by

$$f_i = \mu U_R^2 \int_0^1 \left(f_L - w' f_D + w'' \int_s^1 f_D \, \mathrm{d}s \right) \phi_i \, \mathrm{d}s. \tag{20}$$

The constant coefficients A_i, B_{imnl} and C_{imnl} are given by

$$A_i = \beta_i^4, \tag{21}$$

$$B_{imnl} = \int_0^1 \phi_i (\phi_m'''' \phi_n' \phi_l' + 4\phi_m' \phi_n'' \phi_l''' + \phi_m'' \phi_n'' \phi_l'') \, \mathrm{d}s, \tag{22}$$

$$C_{imnl} = \int_0^1 \phi_i' \phi_m' \left[\int_s^1 \left(\int_0^\eta \phi_n' \phi_l' \, \mathrm{d}\zeta \right) \mathrm{d}\eta \right] \mathrm{d}s, \tag{23}$$

where β_i is the ith dimensionless eigenfrequency of a cantilevered beam [26].

2.4. Numerical methodology

To formulate a stable, accurate and efficient time-integration scheme for the solution of Eq. (19) is by no means a trivial task, due to the nonlinear inertial terms in the equation. The Houbolt method [27] seems to be the most suitable for obtaining reliable simulation results; it is based on the following two backward approximations at time step $k+1$:

$$\ddot{q}^{k+1} = \frac{\sum_{j=1}^4 a_j q^{k-j+2}}{\Delta\tau^2}, \quad \dot{q}^{k+1} = \frac{\sum_{j=1}^4 b_j q^{k-j+2}}{\Delta\tau}, \tag{24}$$

where $a_{j,j=1,2,3,4} = (2, -5, 4, -1)$ and $b_{j,j=1,2,3,4} = (11/6, -3, 3/2, -1/3)$ for the fourth-order scheme.

Substituting Eqs. (24) into Eq. (19), a set of nonlinear ordinary differential equations for the unknown q_i^{k+1} is obtained,

$$D_i q_i + \lambda_{3i} + E_{imnl} q_m q_n q_l + F_{imnl} \lambda_{2m} q_n q_l + C_{imnl} q_m (\lambda_{2n} \lambda_{2l} + q_n \lambda_{1l}) = \Delta\tau^2 f_i, \tag{25}$$

where the superscript $k+1$ has been dropped for clarity, and the time-dependent coefficients λ_{1i}, λ_{2i} and λ_{3i}, at time step $k+1$, are given by

$$(\lambda_{1i}, \lambda_{2i}, \lambda_{3i})^{k+1} = \left(\sum_{j=2}^4 a_j q_i^{k-j+2}, \sum_{j=2}^4 b_j q_i^{k-j+2}, \lambda_{1i}^{k+1} + \Delta\tau\alpha A_i \lambda_{2i}^{k+1} \right). \tag{26}$$

The constant coefficients D_i, E_{imnl} and F_{imnl} are given by

$$D_i = a_1 + (\Delta\tau^2 + \Delta\tau\alpha b_1) A_i,$$

$$E_{imnl} = (\Delta\tau^2 + 3\Delta\tau\alpha b_1) B_{imnl} + (a_1 + b_1^2) C_{imnl},$$

$$F_{imnl} = \Delta\tau\alpha (B_{imnl} + B_{inml} + B_{ilnm}) + b_1 (C_{ilnm} + C_{inml}). \tag{27}$$

Note that the Houbolt method adopted is a multistep backward scheme; one needs to otherwise obtain the first three steps to start off the solution. In the present paper, the initial conditions in terms of $(q_i^0, \dot{q}_i^0)$ are prescribed at $\tau = 0$, and Eq. (25) with $f_i \equiv 0$ (i.e., the free vibration of the plate) is conveniently utilized to retroactively obtain $(q_i^{-\Delta\tau}, \dot{q}_i^{-\Delta\tau})$ and $(q_i^{-2\Delta\tau}, \dot{q}_i^{-2\Delta\tau})$, step by step.

The generalized force f_i obtained from the fluid dynamics part of the numerical model is assumed to be known when solving the deformed shape of the plate from Eq. (25) (as well as Eq. (7)). Therefore, for each specific time step, a subiteration scheme is used to limit the variation between two successive versions of f_i within a prescribed value as small as 1×10^{-8} in terms of $\max(|\Delta f_i|)$. It should be mentioned that, through extensive tests, it has been found that the subiteration scheme is not necessary for simulations with small μ (say $\mu < 0.8$), if proper numerical parameters and initial conditions are used.

3. System dynamics

3.1. Numerical parameters and initial conditions

There are four parameters in the numerical model of the system: the number of panels N, the number of Galerkin modes M, the time step $\Delta\tau$, and the length of the truncated wake street l_W. The convergence of simulation results with respect to these four numerical parameters was examined, and it was concluded that satisfactory convergence is achieved with $N = 200$, $M = 6$, $\Delta\tau = 1.0 \times 10^{-3}$ and $l_W = 40$ when the mass ratio $\mu < 0.8$. With larger μ, more panels and Galerkin modes and smaller time steps have to be used, and the wake length becomes less important for obtaining satisfactory results; in particular, convergent values of the numerical parameters are $N = 400$, $M = 12$, $\Delta\tau = 5.0 \times 10^{-5}$ and $l_W = 10$ when $\mu \geqslant 0.8$. It should be noted that the solution becomes unstable when the mass ratio $\mu \geqslant 0.8$; however, this difficulty has been overcome by using the added-mass compensation method [28].

The influence of initial conditions on the system dynamics was also extensively tested, from very small initial deformations (for example, $q_1^0 = 1.0 \times 10^{-5}$, $q_{i,i\neq 1}^0 = 0$ and $\dot{q}_i^0 = 0$) to relatively large ones (for example, $q_1^0 = 0.01$ or 0.1, $q_{i,i\neq 1}^0 = 0$ and $\dot{q}_i^0 = 0$), as well as from initial deformations in a single mode to those of combined modes. No dependence of the system dynamics on initial conditions has been observed, even though the hysteresis phenomenon widely reported in experiments [1,19,21,23] strongly suggests the coexistence of two stable states (this will be discussed later in this paper).

3.2. Onset of flutter and post-critical vibrations

There are five non-dimensional control parameters in the fluid–structure system: the mass ratio μ, the reduced flow velocity U_R, the length of the upstream rigid segment l_0, the material damping coefficient α, and the viscous drag coefficient C_D. When the other control parameters are fixed, the system dynamics with respect to U_R is shown in Fig. 4(a,b).

It is seen in Fig. 4(a) that the critical reduced flow velocity is $U_{R_c} = 9.92$. When $U_R < U_{R_c}$, the plate remains in a stable flat state; any small disturbance to the system is attenuated. Flutter occurs when $U_R \geqslant U_{R_c}$. With increasing U_R, the flutter amplitude increases monotonically (as shown in Fig. 4(a)); the flutter frequency first decreases, and then slightly recovers at large U_R (see Fig. 4(b)). The decrease in flutter frequency with increasing U_R is qualitatively contrary to what is observed in experiments [5,19,21,23]. This discrepancy may be attributed to the absence of a proper model for (viscous) drag acting on the oscillating plate; further investigation on this aspect will be conducted later in this paper.

The time histories, phase plane plots and modes of the post-critical vibrations at $U_R = 9.95$ and 11.18 are, respectively, shown in Fig. 4(c–h), and at a moderate value of reduced flow velocity $U_R = 13.78$ are presented in Fig. 5(a,b,e). It is observed that when U_R is close to U_{Rc}, the transient is very long and the system dynamics is almost linear; this may explain the observed small amplitude oscillations at a flow velocity immediately exceeding the critical point (see Ref. [21]). For the specific case of $\mu = 0.2$, the modal form of the oscillation involves travelling waves (no stationary nodes) of roughly second-beam-mode shape; there is a quasi-node located at about three-quarters of the plate length. Note that the second-beam-mode shape can more clearly be observed at low U_R, as shown in Fig. 4(g), where the transverse flutter amplitude and the corresponding longitudinal displacement are relatively small. It can be seen in Figs. 4(g,h) and 5(e) that, as U_R increases, the quasi-node becomes less distinct, while the vibration mode remains qualitatively the same. The time history and phase plane plot of the longitudinal displacement of the plate tip are, respectively, shown in Figs. 5(c) and (d); it can be seen that the longitudinal displacement is always negative. The locus of the plate tip exhibits a figure-of-eight shape as shown in Fig. 5(f); it can be seen in this figure, as well as easily proved using Eq. (2), that the frequency of the longitudinal vibration is always twice that of transverse flutter.

As shown in Fig. 4(a), the current theory predicts a supercritical bifurcation. In experiments, however, flutter commonly occurs in a subcritical manner [1,19,21,23]. All theories to date fail to capture this characteristic; they all predict a supercritical bifurcation. Some further comments on this are made in the Conclusions.

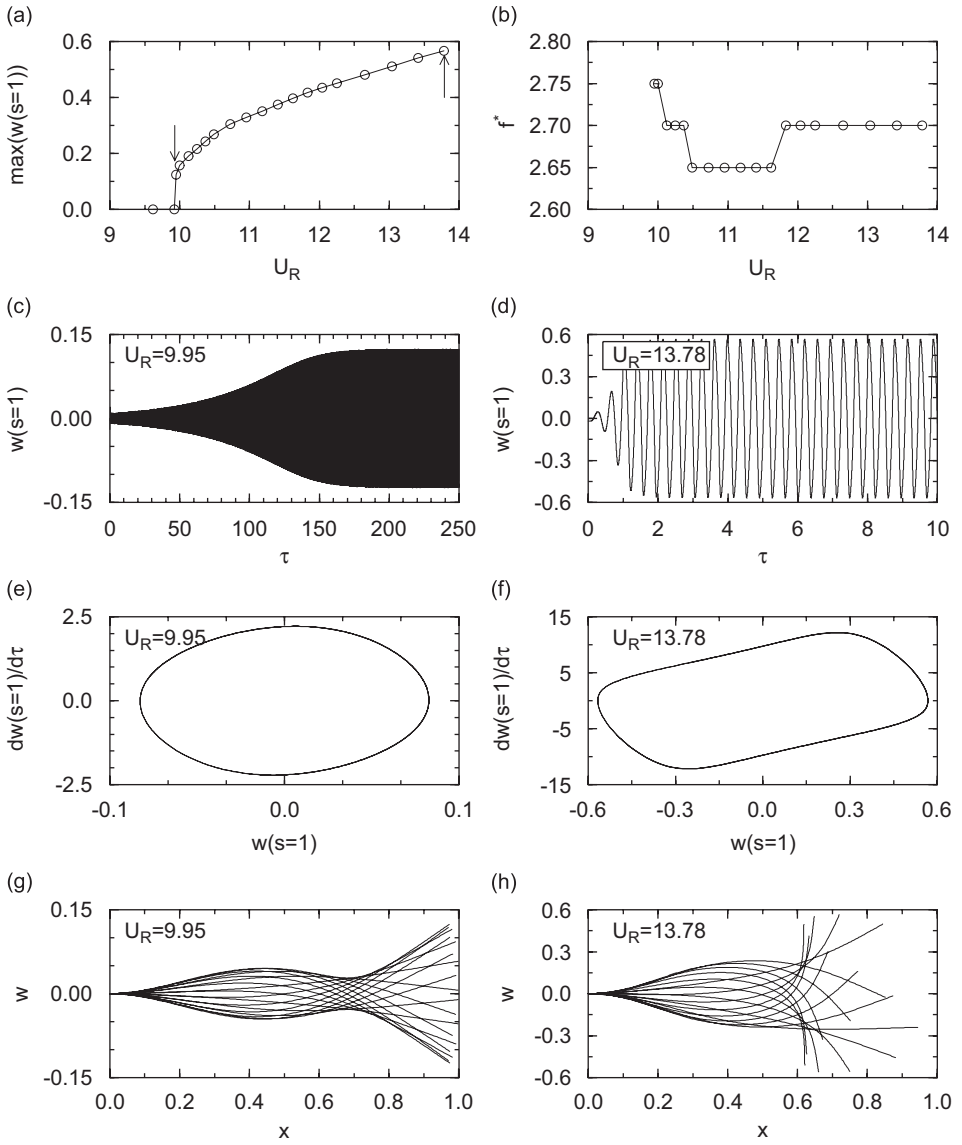

Fig. 4. The instability and post-critical vibrations for $\mu = 0.2$, $l_0 = 0.01$, $\alpha = 0.004$ and $C_D = 0$: (a) the bifurcation diagram; (b) the flutter frequency; (c,d) the time histories; (e,f) the phase plane plots; and, (g,h) the vibration modes.

3.3. *The influence of l_0, α and C_D*

The effect of varying the length of the upstream rigid segment l_0 and the material damping coefficient α on the system dynamics is shown in Figs. 6 and 7.

When the rigid segment is short, disturbances in the flow due to plate motion affect the flow upstream; i.e., the upstream flow cannot be treated as a steady uniform flow. When l_0 is small, say $l_0 < 5$, significant changes occur in the flutter amplitude with small variations of l_0. The critical point also depends on the value of l_0. In particular, as shown in Fig. 7, $U_{R_c} = 9.20$ when $l_0 = 1.0$; while $U_{R_c} = 9.92$ when $l_0 = 0.01$. When l_0 is sufficiently large, the dependence of the system dynamics on it becomes unimportant; eventually, U_{R_c} converges to the value for $l_0 = \infty$. It is also found that the influence of l_0 on the system dynamics becomes less important when the mass ratio μ is large, as shown in Fig. 7.

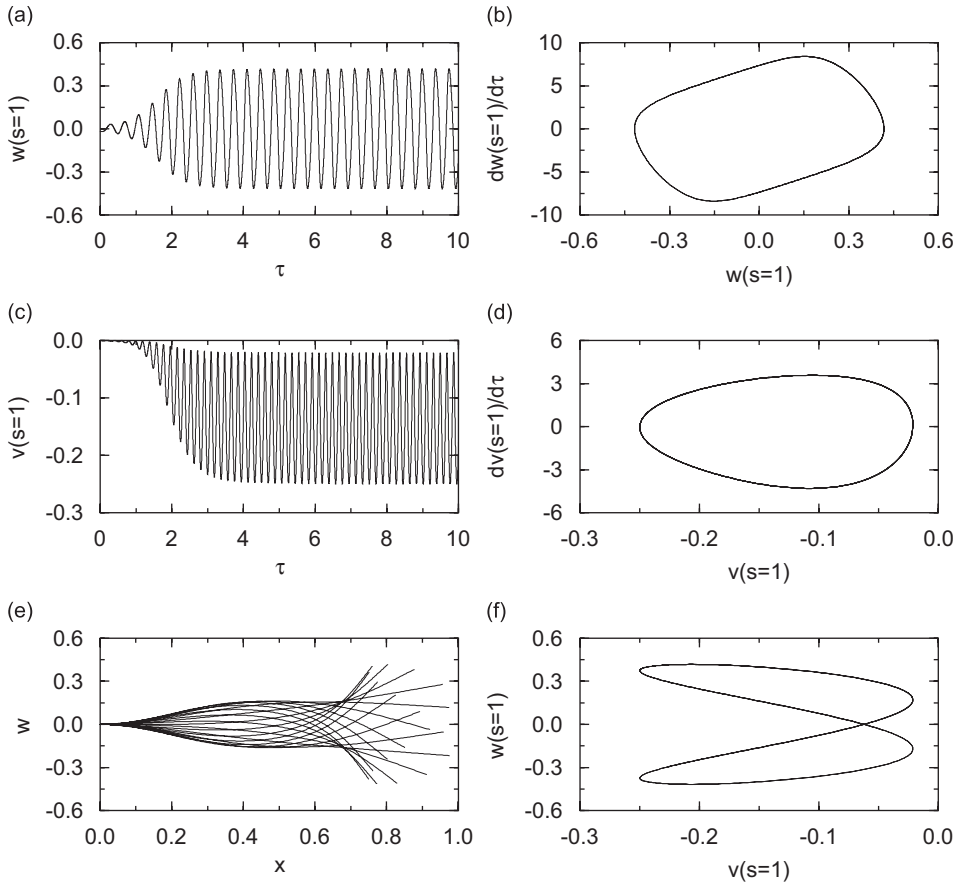

Fig. 5. The post-critical dynamics for $\mu = 0.2$, $U_R = 11.83$, $l_0 = 0.01$, $\alpha = 0.004$ and $C_D = 0$. (a,b) The time history and phase plane plot of the transverse displacement of the tip, respectively; (c,d) the time history and phase plane plot of the longitudinal displacement of the tip, respectively; (e) the vibration mode of the plate; and, (f) the locus of the tip motion.

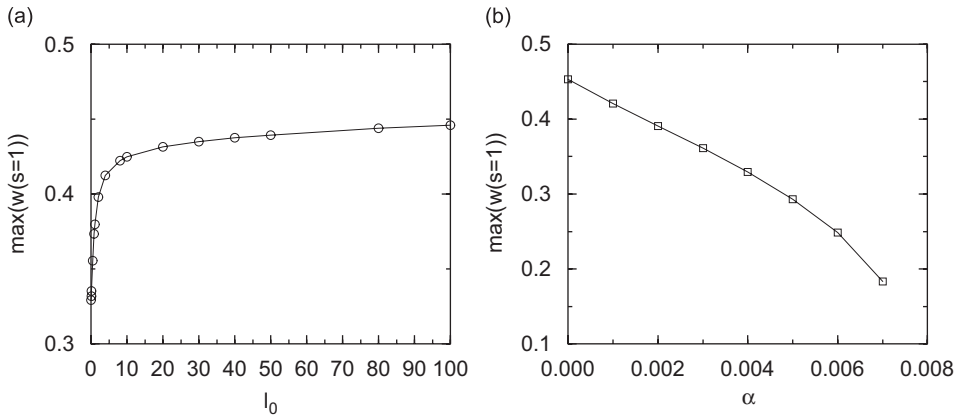

Fig. 6. The influence of l_0 and α on the flutter amplitude: (a) flutter amplitude versus the length of the upstream rigid segment l_0, and (b) flutter amplitude versus the material damping coefficient α. The reference parameter set is $\mu = 0.2$, $U_R = 10.95$, $C_D = 0$, $l_0 = 0.01$ and $\alpha = 0.004$.

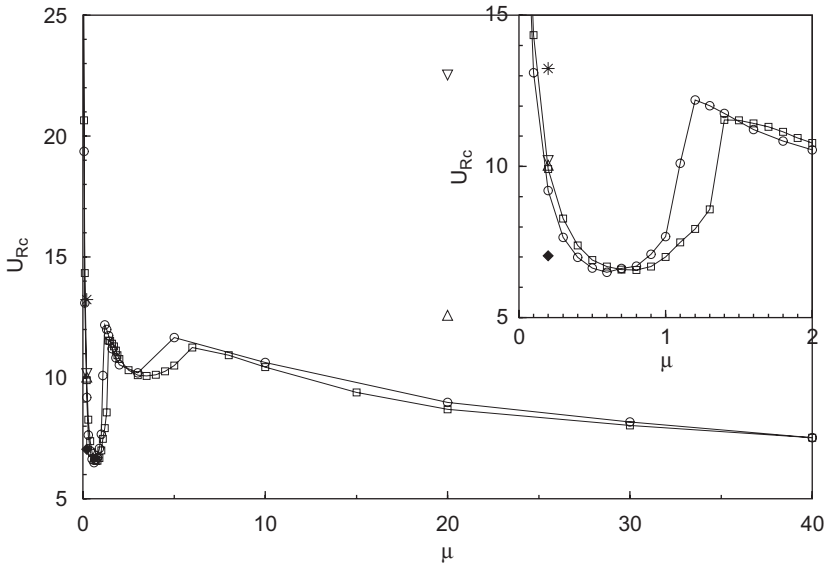

Fig. 7. The influence of l_0, α and C_D on the critical point: —○—, $l_0 = 1.0$, $\alpha = 0.004$, $C_D = 0$; —□—, $l_0 = 0.01$, $\alpha = 0.004$, $C_D = 0$; ◆, $l_0 = 1.0$, $\alpha = 0.001$, $C_D = 0$; △, $l_0 = 0.01$, $\alpha = 0.004$, $C_D = 0.05$; ▽, $l_0 = 0.01$, $\alpha = 0.004$, $C_D = 0.1$; ∗, $l_0 = 0.01$, $\alpha = 0.004$, $C_D = 0.8$.

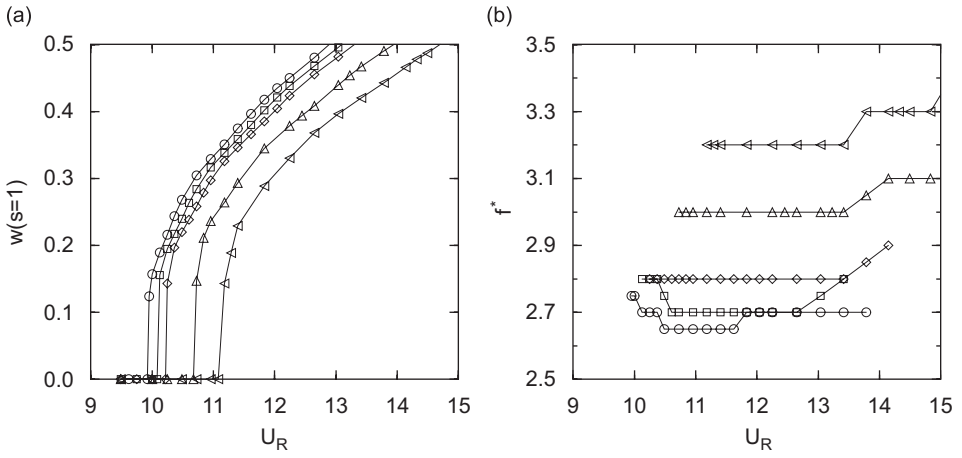

Fig. 8. (a) The flutter amplitude and (b) frequency of the system with various values of C_D: —○—, $C_D = 0$; —□—, $C_D = 0.1$; –◇—, $C_D = 0.2$; —△—, $C_D = 0.5$; —◁—, $C_D = 0.8$. The other parameters used are $\mu = 0.2$, $l_0 = 0.01$ and $\alpha = 0.004$.

On the other hand, as expected, the flutter amplitude becomes smaller when the system has a larger material damping α. The critical point also depends on the value of α: as shown Fig. 7 for the case of $\mu = 0.2$, $l_0 = 1.0$ and $C_D = 0$, $U_{R_c} = 7.05$ when $\alpha = 0.001$; while, $U_{R_c} = 9.20$ when $\alpha = 0.004$.

When taking into account the viscous drag C_D, the system becomes more stable, the flutter amplitude is reduced and the flutter frequency increases, as shown in Figs. 7 and 8. It was observed in the experiments of Taneda [5] that the value of the fluid-dynamic drag, if evaluated in terms of an equivalent drag coefficient C_D, was about 0.07 before flutter took place and it jumped to about 1.0 at the critical point. Omitting the viscous drag will considerably underestimate the value of the critical point. In particular, as shown in Fig. 8(a), the critical reduced flow velocity $U_{R_c} = 9.92$ when $C_D = 0$, while $U_{R_c} = 11.08$ when $C_D = 0.8$. Another important role of the viscous drag C_D is to increase the flutter frequency; this is expected, because the tension in the plate is related to the viscous drag according to Eqs. (4) and (17).

It can be shown that varying l_0 and α has little effect on the flutter frequency; but C_D does have a significant effect. As shown in Fig. 8(b), the flutter frequency at the critical point is $f_c^\star = 2.75$ when $C_D = 0$; it grows monotonically to $f_c^\star = 3.15$ when $C_D = 0.8$. For the specific system with $\mu = 0.232$ experimentally studied by Kornecki et al. [11], it has been found that $f_c^\star = 2.7$ when $C_D = 0$; while $f_c^\star = 3.1$ when $C_D = 0.8$, which agrees very well with the experimental measurement.

However, it is noticed that, when C_D is fixed, the flutter frequency may be invariant or even decrease with increasing U_R, as shown in Fig. 8(b) as well as Fig. 4(b); this is contradictory to experimental observations [5,19,21,23]. This observation suggests that the value of C_D should be dependent on the flutter amplitude: the larger the U_R, the larger is the flutter amplitude (see Fig. 4(a)), and the larger the value of C_D.

3.4. On the hysteresis phenomenon and the subcritical bifurcation

Hysteresis phenomena have repeatedly been reported in previous experimental observations [1,19,21,23]. In general, it has been observed that flutter takes place in an abrupt manner: once the flow velocity reaches a critical point, vibration develops suddenly with a large amplitude. On the other hand, when the plate is already in vibration and the flow velocity is gradually reduced, the plate may return to rest at another critical point, lower than the former one. Therefore, a hysteresis loop is formed; i.e., the bifurcation leading to flutter is subcritical. This hysteresis phenomenon also implies that the dynamics depends on initial conditions; two stable states coexist between the lower and the upper critical points.

As already remarked, no existing theory is capable of predicting subcritical dynamic behaviour in the flow-induced flutter. Clearly, this must be due to either a systemic weakness in all the theoretical models, or because a particular aspect of all (or virtually all) experiments, is not taken into account in the theoretical models.

In all experiments, the plate is of course three-dimensional. Thus, the theoretical assumption that the flow is two-dimensional ignores all edge-effects, e.g. edge-vortices, the overall effect of which may not be negligible; there may indeed be a phase lag between their generation and the plate motion. Also, most of the fluid-dynamics models employed are linear, and the observed hysteresis may be due to fluid nonlinearities. However, simulations using Navier–Stokes solvers have not shown any hysteresis effects either; still, this may have been insufficiently explored.

On the purely experimental side of things, it is noted that all experiments have been conducted in a wind or water tunnel; yet, the effect of confinement was not considered. Furthermore, this effect is not a straightforward blockage when the plate is fluttering. Recently, for the problem of vortex-induced vibrations of an oscillating cylinder, Prasanth et al. [29] have shown that a blockage of 5% as compared to 1% has a profound effect on the dynamics – affecting lock-in and the existence of hysteresis; but both 1% and 5% are normally considered "small". Clearly, this is not a static effect of increasing the effective flow velocity around the cylinder, but a more profound effect on the vortical dynamics. In the case of the plate, the amplitudes of motion are larger at the trailing edge than for the cylinder, and so also is the dynamic blockage; hence this effect could well be more pronounced.

Some of these possible causes of the observed hysteresis are currently under investigation. In the remarkable experiments by Zhang et al. [1], it has been observed that the onset of the flutter of a cantilevered plate in axial flow is accompanied by the evolution of the vortical wake from a von Kármán type to an undulating one. To demonstrate how a hysteresis might occur due to vortical effects, we have investigated (as a preliminary exercise) the effect of adding a steady von Kármán-type vortex street to the undulating wake vortices shed at the trailing edge while in motion; specifically, it is assumed that $\Gamma_V = UL$ for small motions (when $W(S = L)/L \leqslant 0.02$) and $\Gamma_V = 0$ for larger motions (when $W(S = L)/L > 0.02$), where Γ_V is the strength of a single von Kármán wake vortex. The geometry of the von Kármán wake street is set as $S_V/L = 0.1$ and $D_V/L = 0.02$, where S_V is the distance between two successive vortices in the same row and D_V is the distance between either of the two vortex rows to the neutral plane. The result is shown in Fig. 9, demonstrating that a hysteresis may be obtained. It is stressed that the mechanism here is non-physical, and only exploratory from the phenomenological point of view; (furthermore, it is not used in the calculations presented in what follows).

Although not investigated in this paper, some further thoughts as to the nature of the discrepancy between theory (predicting supercritical onset of flutter) and experiment (subcritical onset with considerable hysteresis)

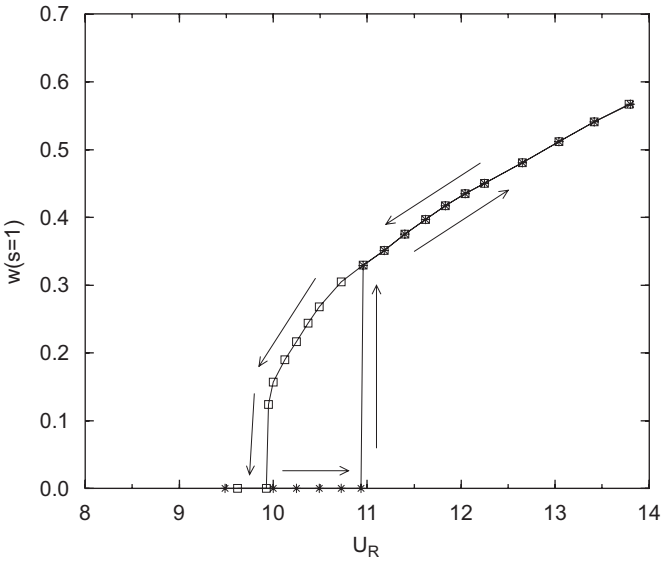

Fig. 9. The bifurcation diagram of the system with the additional consideration of a von Kármán wake. The other parameters used are $\mu = 0.2$, $l_0 = 0.01$, $\alpha = 0.004$ and $C_D = 0$. Initial conditions: —□—, $q_1 = -1.0 \times 10^{-2}$; and, —∗—, $q_1 = -1.0 \times 10^{-5}$; the other parts of the initial conditions are $q_{i,i\neq 1} = 0$ and $\dot{q}_i = 0$.

may be useful. One possibility is that the usually limited size of the test-section cross-section in most experiments and the resulting interaction of the wake with the wind/water tunnel walls may be responsible. Another possibility is that, due to quasi-ubiquitous imperfections, spanwise bending would stiffen a plate in experiments prior to the onset of flutter, but such bending could be partly ironed out at post-critical flows, thus generating a hysteresis.

3.5. Dynamics of the system with various μ

In Fig. 10, we examine the flutter boundary in terms of the mass ratio μ. The flutter boundaries predicted by other theories [2,14,16,17,20,23] and the corresponding published experimental data [11,14,18,19,21] are also presented. The present theory is found to be in better agreement with the experimental data than can be achieved by other theories.

In Fig. 10, U_R/μ is used as the ordinate, which can be written as $U_R/\mu = [(\rho_P h)^{3/2}/(\rho_F D^{1/2})]U$. Moreover, the mass ratio μ can be written as $[\rho_F/(\rho_P h)]L$. Therefore, Fig. 10 actually reveals the relation between the critical flow velocity U_c and the plate length L, the most controllable parameter in experiments, when the other physical parameters (ρ_P, ρ_F, h and D) of the fluid–structure system are fixed.

All the theoretical and experimental data presented in Fig. 10 indicate the same trend for the flutter boundary: when the plate is short, U_c is very sensitive to L; while, when the plate is sufficiently long, U_c is almost a constant. In general, U_c decreases with increasing L. However, within the range $1.0 < \mu < 1.2$, there is a local rise and then subsidence in U_c as L increases; a subtle transition in the flutter mode shape occurs in this interval (refer to Figs. 12(c) and (d) to see the difference between the vibration modes when $\mu = 1.1$ and 1.2, respectively).

As for the large scatter in the experimental data shown in Fig. 10, we attribute this to the difficulty encountered in setting up the experiments. Moreover, the plates used in different experiments have different aspect ratios, different lengths of upstream rigid segment, different levels of internal damping, and the experiments themselves have been carried out in different wind or water tunnels with different geometries; all these factors will cause variations in U_c. Nevertheless, it is very interesting to notice that most theoretical predictions are in better agreement with most experimental data when μ is large. This implies that all the possible factors mentioned above have much less influence on the stability of the system when the plate is long.

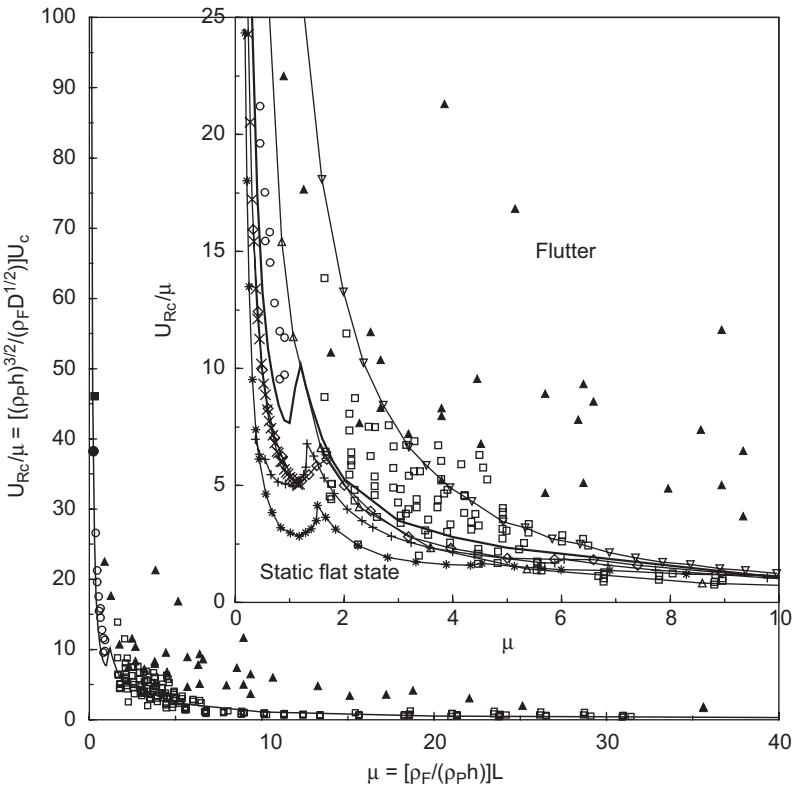

Fig. 10. The flutter boundary in terms of mass ratio μ: ——, present theory; •, experimental data of Kornecki et al. [11]; ○, experimental data of Huang [14]; □, experimental data of Yamaguchi et al. [18]; ▲, experimental data of Watanabe et al. [19]; ■, experimental data of Tang et al. [21]; —×—, theory of Huang [14]; —∗—, theory of Yamaguchi et al. [17]; —◇—, theory of Watanabe et al. [20]; —+—, theory of Guo and Païdoussis [16]; —△—, theory of Shelley et al. [23]; —▽—-, theory of Argentina et al. [2]. In the present theory, the calculations have been conducted for $l_0 = 1.0$, $\alpha = 0.004$ and $C_D = 0$.

Along the flutter boundary shown in Fig. 10, the flutter frequencies $f_c^\star$ at various values of μ have been obtained and presented in Fig. 11. Similar to Fig. 10, the purpose here is to reveal the relation between f_c and L when the other physical parameters (ρ_P, ρ_F, h and D) of the system are fixed, Fig. 11 uses $f_c^\star/\mu^2 = [(\rho_P h)^{5/2}/(\rho_F^2 D^{1/2})]f_c$ as ordinate, and μ is written as $[\rho_F/(\rho_P h)]L$. It can be seen in Fig. 11 that $f_c^\star$ has the same trend as U_c in Fig. 10: f_c is very sensitive to L for short plates, and it is almost invariant for long plates; f_c generally decreases as L increases, but there is a local rise and then subsidence for $1.0 < \mu < 1.2$. The experimental measurements of the frequencies at the flutter boundary made by Kornecki et al. [11], Huang [14] and Tang et al. [21] are also presented in Fig. 11; it can be seen that the present theory agrees with experimental observations very well. It should be noted that, due to the difference in the normalization methods used and the lack of exact values for the physical parameters of the system, the experimental results obtained by Yamaguchi et al. [18] and Watanabe et al. [19], as well as all the previous theoretical predictions for f_c, cannot be included in Fig. 11.

Flutter modes of the system with different values of mass ratio μ, obtained at the corresponding critical points U_{R_c}, are shown in Fig. 12. We have found through tests that, for a given μ, the flutter mode of the system at different post-critical flow velocities is qualitatively the same, although the vibration amplitude and some other aspects (for example, the location and girth of the quasi-node) may vary. As shown in Fig. 13, when comparing these vibration modes with the experimental observations by Tang et al. [21] for $\mu = 0.30$ and Watanabe et al. [19] for $\mu = 2.7$ and 35.7, good agreement is found. It can be seen from Fig. 12 that, as μ increases more and more, higher-order modes participate in the dynamics and they become increasingly significant. It is also interesting to see that a pure first-mode flutter never happens for any value of μ; cf. Ref. [4].

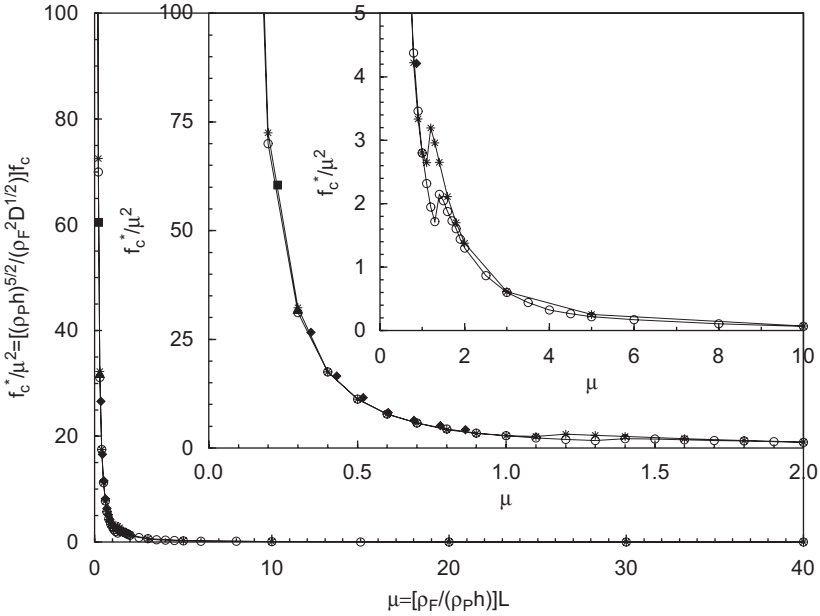

Fig. 11. The flutter frequencies of the plate along the boundary of instability in terms of mass ratio μ: —○—, present theory, $l_0 = 0.01$; —∗—, present theory, $l_0 = 1.0$; □, experimental data of Kornecki et al. [11]; ◆, experimental data of Huang [14]; ▲, experimental data of Tang et al. [21]. In the present theory, the calculations have been conducted for $\alpha = 0.004$ and $C_D = 0$.

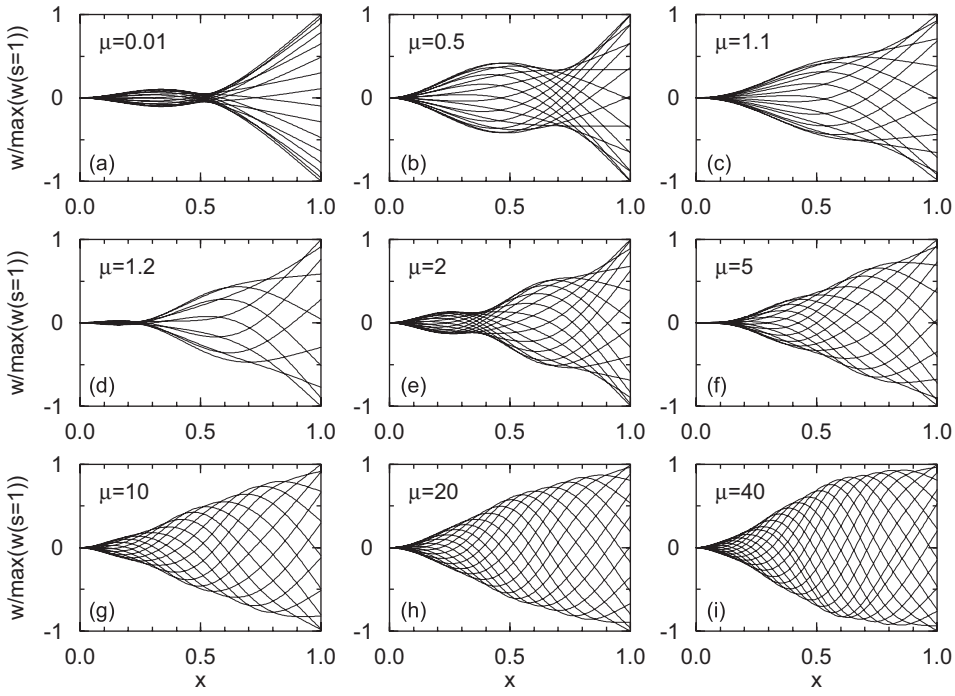

Fig. 12. Vibration modes of the system for different values of mass ratio μ obtained at the corresponding critical points U_{R_c}: (a) $\mu = 0.01$; (b) $\mu = 0.5$; (c) $\mu = 1.1$; (d) $\mu = 1.2$; (e) $\mu = 2$; (f) $\mu = 5$; (g) $\mu = 10$; (h) $\mu = 20$; (i) $\mu = 40$.

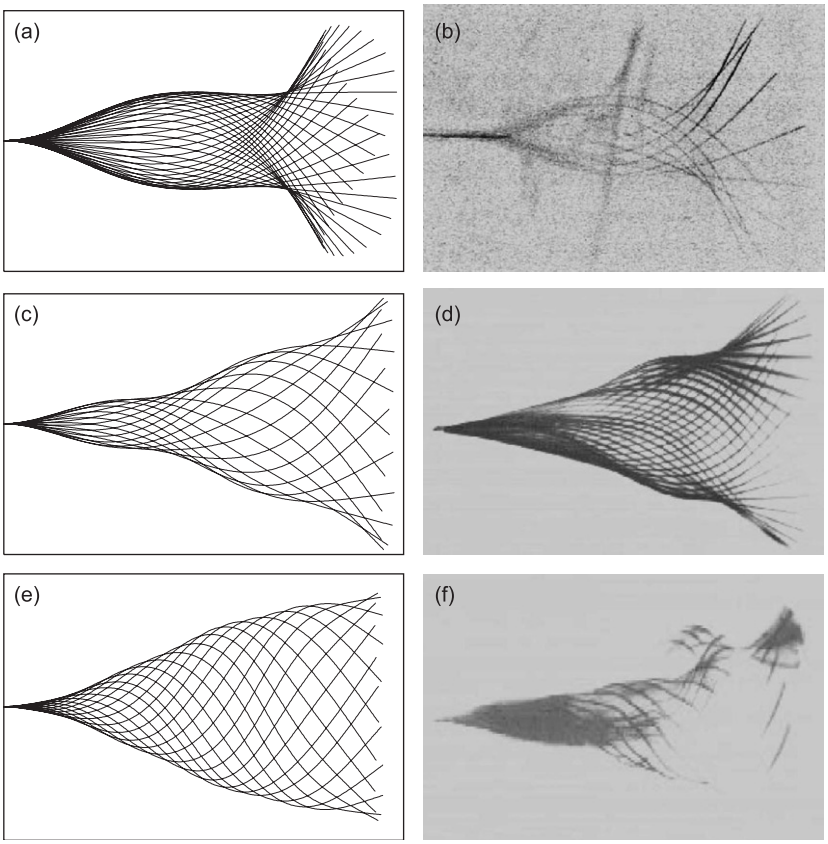

Fig. 13. The vibration modes at various values of μ predicted by the present theory and observed in previous experiments: (a,c,e) predicted by the present theory; (b,d,f) observed in previous experiments. (a,b) For the system with a small μ studied by Tang et al. [21], $\mu = 0.30$; (c,d) for the system with a medium μ studied by Watanabe et al. [19], $\mu = 2.7$; (e,f) for the system with a large μ studied by Watanabe et al. [19], $\mu = 35.7$.

4. Conclusions

In this paper, a nonlinear equation of motion of the plate is developed using the assumption of inextensibility of the centreline; the longitudinal displacement of the plate has been taken into account. Also, an unsteady lumped vortex model is used to calculate the pressure difference across the plate. The pressure difference is then decomposed into a lift force and an inviscid drag force. A viscous drag coefficient is also independently considered in the model. The fluid loads thus obtained are coupled with the plate equation of motion.

The analysis of the system dynamics is carried out in the time-domain. Not only the flutter boundary but also the post-critical behaviour of this fluid–structure system have been investigated. Through extensive numerical simulations, various factors affecting the system dynamics, such as the upstream rigid segment length, the material damping and the viscous drag, have been carefully studied.

A flutter boundary is obtained in the form of critical flow velocity versus the length of the flexible plate. It is found that the critical flow velocity is very sensitive to plate length when the plate is short, while it is almost invariant when the plate is sufficiently long; cf. Ref. [30]. Normally, a longer plate has a lower critical flow velocity. However, in some parameter ranges the critical flow velocity may become locally higher with increasing plate length. The flutter boundary and flutter frequencies/modes obtained using the present theory are compared with available experimental data and the results of other theories. The current theory achieves better agreement with the experimental data than other theories.

Finally, the most important discrepancy between the present theory, indeed *all* theories, and experiment has been discussed in Section 3.4, namely the fact that theory predicts a supercritical onset of flutter, while experiment in most cases that it is subcritical, with a strong hysteresis. Although no definite resolution of this discrepancy has been achieved, some useful comments and suggestions are offered.

Acknowledgements

The authors gratefully acknowledge the support by the Natural Sciences and Engineering Research Council of Canada (NSERC) and Le Fonds Québécois de la Recherche sur la Nature et les Technologies (FQRNT); the leading author also gratefully acknowledges the support by a NSERC scholarship.

References

[1] J. Zhang, S. Childress, A. Libchaber, M. Shelley, Flexible filaments in a flowing soap film as a model for one-dimensional flags in a two-dimensional wind, *Nature* 408 (2000) 835–839.
[2] M. Argentina, L. Mahadevan, Fluid-flow-induced flutter of a flag, *Proceedings of the National Academy of Science of the United States of America* 102 (2005) 1829–1834.
[3] E.H. Dowell, *Aeroelasticity of Plates and Shells*, first ed., Noordhoff International Publishing, Leyden, 1975.
[4] M.P. Païdoussis, *Fluid–Structure Interactions. Slender Structures and Axial Flow*, first ed., Vol. 2, Elsevier Academic Press, London, 2004.
[5] S. Taneda, Waving motions of flags, *Journal of the Physical Society of Japan* 24 (1968) 392–401.
[6] S.K. Datta, W.G. Gottenberg, Instability of an elastic strip hanging in an airstream, *Journal of Applied Mechanics* 42 (1975) 195–198.
[7] J. Katz, A. Plotkin, *Low-Speed Aerodynamics*, second ed., Cambridge University Press, New York, 2001.
[8] Y. Yadykin, V. Tenetov, D. Levin, The flow-induced vibration of a flexible strip hanging vertically in a parallel flow, part 1: temporal aeroelastic instability, *Journal of Fluids and Structures* 15 (2001) 1167–1185.
[9] C. Semler, G.X. Li, M.P. Païdoussis, The non-linear equations of motion of pipes conveying fluid, *Journal of Sound and Vibration* 165 (1992) 577–599.
[10] C. Lemaitre, P. Hémon, E. de Langre, Instability of a long ribbon hanging in axial air flow, *Journal of Fluids and Structures* 20 (2005) 913–925.
[11] A. Kornecki, E.H. Dowell, J. O'Brien, On the aeroelastic instability of two-dimensional panels in uniform incompressible flow, *Journal of Sound and Vibration* 47 (1976) 163–178.
[12] R.L. Bisplinghoff, H. Ashley, R.L. Halfman, *Aeroelasticity*, first ed., Addison-Wesley, Reading, MA, 1955.
[13] L.K. Shayo, The stability of cantilever panels in uniform incompressible flow, *Journal of Sound and Vibration* 68 (1980) 341–350.
[14] L.X. Huang, Flutter of cantilevered plates in axial flow, *Journal of Fluids and Structures* 9 (1995) 127–147.
[15] T. Balint, A.D. Lucey, Instability of a cantilevered flexible plate in viscous channel flow, *Journal of Fluids and Structures* 20 (2005) 893–912.
[16] C.Q. Guo, M.P. Païdoussis, Stability of rectangular plates with free side-edges in two-dimensional inviscid flow, *Journal of Applied Mechanics* 67 (2000) 171–176.
[17] N. Yamaguchi, K. Yokota, Y. Tsujimoto, Flutter limits and behaviors of a flexible thin sheet in high-speed flow—I: analytical method for prediction of the sheet behavior, *ASME Journal of Fluids Engineering* 122 (2000) 65–73.
[18] N. Yamaguchi, T. Sekiguchi, K. Yokota, Y. Tsujimoto, Flutter limits and behaviors of a flexible thin sheet in high-speed flow—II: experimental results and predicted behaviors for low mass ratios, *ASME Journal of Fluids Engineering* 122 (2000) 74–83.
[19] Y. Watanabe, S. Suzuki, M. Sugihara, Y. Sueoka, An experimental study of paper flutter, *Journal of Fluids and Structures* 16 (2002) 529–542.
[20] Y. Watanabe, K. Isogai, S. Suzuki, M. Sugihara, A theoretical study of paper flutter, *Journal of Fluids and Structures* 16 (2002) 543–560.
[21] D.M. Tang, H. Yamamoto, E.H. Dowell, Flutter and limit cycle oscillations of two-dimensional panels in three-dimensional axial flow, *Journal of Fluids and Structures* 17 (2003) 225–242.
[22] P.J. Attar, E.H. Dowell, D.M. Tang, Modeling aerodynamic nonlinearity for two aeroelastic configurations: delta wing and flapping flag, *Proceedings of the 44th AIAA/ASME/ASCE/AHS Structures, Structural Dynamics, and Materials Conference, 7–10 April*, Norfolk, VA, 2003, pp. 1–12.
[23] M. Shelley, N. Vandenberghe, J. Zhang, Heavy flags undergo spontaneous oscillations in flowing water, *Physical Review Letters* (094302) (2005) 1–4.
[24] D.G. Crighton, J.E. Oswell, Fluid loading with mean flow. i. Response of an elastic plate to localized excitation, *Philosophical Transactions of Royal Society of London* 335 (1991) 557–592.
[25] J.C. Snowdon, *Vibration and Shock in Damped Mechanical Systems*, first ed., Wiley, New York, 1968.
[26] R.E.D. Bishop, D.C. Johnson, *The Mechanics of Vibration*, Cambridge University Press, Cambridge, 1979.

[27] C. Semler, W.C. Gentleman, M.P. Païdoussis, Numerical solutions of second order implicit non-linear ordinary differential equations, *Journal of Sound and Vibration* 195 (1996) 553–574.
[28] F. Bélanger, M.P. Païdoussis, E. de Langre, Time-marching analysis of fluid-coupled system with large added mass, *AIAA Journal* 33 (1995) 752–755.
[29] T.K. Prasanth, S. Behara, S.P. Singh, R. Kumar, S. Mittal, Effect of blockage on vortex-induced vibrations at low reynolds number, *Journal of Fluids and Structures* 22 (2006) 865–876.
[30] E. de Langre, M.P. Païdoussis, O. Doaré, Y. Modarres-Sadeghi, Flutter of long flexible cylinders in axial flow, *Journal of Fluid Mechanics* 571 (2007) 371–389.